Spectrochimica Acta Part B 66 (2011) 67–73

Contents lists available at ScienceDirect

Spectrochimica Acta Part B

journal homepage: www.elsevier.com/locate/sab

# Wavelength-dispersive spectral analysis and quantification of monazites by electron-probe microanalysis

E. Sánchez [a,b], A.C. Carreras [b,c,1], A.B. Guereschi [b,d], R.D. Martino [b,d], G. Castellano [b,e,*]

[a] INQUISAL, Universidad Nacional de San Luis, CC 290, (5700) San Luis, Argentina
[b] CONICET, Argentina
[c] NTEQUI, Universidad Nacional de San Luis, CC 290, (5700) San Luis, Argentina
[d] FCEFyN, Universidad Nacional de Córdoba, Ciudad Universitaria, (5016) Córdoba, Argentina
[e] FaMAF, Universidad Nacional de Córdoba, Medina Allende s/n, Ciudad Universitaria, (5016) Córdoba, Argentina

ARTICLE INFO

*Article history:*
Received 20 October 2010
Accepted 10 December 2010
Available online 17 December 2010

*Keywords:*
EPMA
Monazite
Mineral chemistry
Peak overlapping

ABSTRACT

The problem of determining the chemical composition of monazite grains through electron probe microanalysis is studied, by using a scanning electron microscope with a wavelength dispersive spectrometer. A careful qualitative analysis is performed with the purpose of determining all the elements present in the samples, the lines to be used in the quantifications trying to minimize interferences, the angular positions and the acquisition times for the measurement of peak and background intensities and the crystals to be used. Particular emphasis is devoted to the analysis of Th, U and Pb, which are used to determine the age of the rock by means of the U–Th–Pb method, commonly used in geochronology. Quantitative determinations of the chemical composition of monazite grains are performed, optimizing the experimental conditions on the basis of the qualitative analysis. The determinations were made under two different criteria of quantification of oxygen, and the dissimilar results obtained are discussed.



## 1. Introduction

Electron probe microanalysis (EPMA) is a powerful analytical tool, useful in the study of materials of different characteristics. When a highly collimated electron beam impinges on a material, a number of interactions occurs, which give rise to the different signals registered in an electron microprobe [1,2]. The wide range of possible energy losses drive electrons to a lateral spreading of trajectories, exceeding the dimensions of the surface initially covered by the primary beam [3]. Anyway, these features allow electron probes to attain chemical quantitative analyses of the elements present in a very small region of a sample, along a wide range of specimen compositions [1,3]. The interaction volume determines the spatial resolution of this technique, usually of the order of 5 $\mu m^3$, which depends on the incident beam energy, the sample composition and the nature of the signals considered [4]. Traditional quantification methods are restricted to the case of flat homogeneous samples, but the characterization of micrometric inhomogeneities has scarcely been faced [5–8].

The accuracy attained in EPMA is of particular interest in the analysis of minerals, where small variations of elemental concentrations may strongly influence the conclusions drawn regarding the characteristics of a specific sample. The importance of this issue becomes more evident in the case of monazites, which are the basis of a number of studies in geochronology [9]. Among several components that appear in monazites, traces of lead and uranium in combination with minor thorium concentrations are used for determining the age of a rock from the U–Th–Pb method [10], commonly used in geochronology. U–Th–Pb chronometers are probably the most accurate ones for geological materials older than 30 Ma (millions of years ago). This dating method is based on the calculation of ages from the concentrations in which these elements are found in the mineral, according to the following disintegration scheme: $^{235}U \rightarrow {}^{206}Pb$; $^{238}U \rightarrow {}^{207}Pb$; and $^{232}Th \rightarrow {}^{208}Pb$. The isotope $^{204}Pb$ is the stable Pb isotope, and the age of a rock is estimated from the closure of the U–Th–Pb system in the mineral, given reasonable assumptions regarding the initial Pb isotopic ratio. The validity of this method depends on the following requirements: the mineral has always remained closed for U, Th, Pb and all the daughters of the intermediate reaction series; accurate values for the initial Pb isotopic ratio; accurate disintegration constant; the isotopic composition of U should be normal, i.e. no evidence of splitting or fission; and systematic analytical errors must be strongly avoided.

Geochronology studies through the analysis of monazite samples apply to magmatic and polimetamorphic events due to their high Th and U content, and to the fact that only radiogenic Pb is present, whose composition increases with time [11], so that the requirements

* Corresponding author. FaMAF, Universidad Nacional de Córdoba, Medina Allende s/n, Ciudad Universitaria, (5016) Córdoba, Argentina. Tel.: +54 351 4334051; fax: +54 351 4334054.
*E-mail address:* gcas@famaf.unc.edu.ar (G. Castellano).
[1] Now at: FaMAF, Universidad Nacional de Córdoba, Medina Allende s/n, Ciudad Universitaria, (5016) Córdoba, Argentina.

0584-8547/$ – see front matter © 2010 Elsevier B.V. All rights reserved.
doi:10.1016/j.sab.2010.12.004

listed above for using this dating method are met. Monazite U–Th–Pb EPMA dating is an accurate in situ geochronological technique [9,12], providing valuable dating results even if monazites have suffered metamorphic events involving the fluid interaction and recrystallisation [13].

Some authors have shown [9,14–19] that EPMA is the best method for detecting very small scale inhomogeneities, in view of its high spatial resolution (1–2 μm), allowing to demonstrate the lack of significant diffusion processes at 700 °C [9], and even at 900 °C [20]. The effect of fluid–mineral interaction is usually limited to areas near fractures and crystal defects, so the pristine magmatic monazite and subsequent metamorphic events can be dated separately.

Monazite [(Ce,La,Nd,Pr,Th,Y)$PO_4$] is a phosphate which contains rare earth elements (REE), and usually is found as a small isolated crystal. There are at least four different kinds of monazites, which are classified according to their major composition: monazite-(Ce) [(Ce,La,Pr,Nd)$PO_4$], monazite-(La) [(La,Ce,Nd,Pr)$PO_4$], monazite-(Nd) [(Nd,La,Ce,Pr)$PO_4$], monazite-(Pr) [(Pr,Nd,Ce,La)$PO_4$], etc. In this notation, the bracket lists elements in order of decreasing concentration. $SiO_2$ usually appears in small amounts, as well as other elements, among them thorium, lead and uranium, which allow to determine the age of the rock from the U–Th–Pb method.

In several works devoted to the suitability of the U–Th–Pb dating method (see e.g. [10,21]), elemental concentrations in the monazite are assessed by using mainly the most intense emission lines. However, the REE have their characteristic L X-ray energies very close, presenting a number of peak overlaps with different elements. In addition, minor elements also exhibit interferences with the most intense characteristic X-ray peaks, being most important for U, Pb and Y. A critical example of considering the most intense lines is the case of Pb-M$\alpha$, since it is superimposed with the Y-L$\gamma_{2,3}$ emission line. Generally, the most intense Y-L$\alpha$ line is measured and the proportion corresponding to the Y-L$\gamma_{2,3}$ is assessed, thus deducing its contribution to the Pb-M$\alpha$ line intensity. This approach involves certain systematic error, since L$\alpha_1$ and L$\alpha_2$ lines respectively correspond to decays from $M_5$ and $M_4$ subshells to $L_3$ subshell, whereas L$\gamma_2$ and L$\gamma_3$ lines respectively correspond to decays from $N_2$ and $N_3$ subshells to $L_1$ subshell [22]. This means that the ratio between the corresponding intensities depends on the incident electron beam energy, and the uncertainty in this ratio may influence the value obtained for the intensity of the Y-L$\gamma_{2,3}$, the resulting concentration of lead not being therefore entirely reliable.

The aim of the present work is to contribute with clear strategies for monazite characterization by EPMA, through a careful analysis of a number of overlapping effects in the elements present in it, selecting the most suitable emission lines for quantification. This purpose implies to minimize uncertainties in the characteristic intensities, allowing accurate dating through the U–Th–Pb method mentioned above. As shown below, the procedure proposed here implies quantification of Pb through its M$\beta$ line, since no superposition with other elements is observed. This methodology will be exemplified here through the characterization of a thin section from the rock sample SL 29, from Sierra de Comechingones, near Cañada de Álvarez, Córdoba, Argentina [23], a sample from high-grade metamorphic rocks.

## 2. Experimental

The sample consisted of a polished rock thin section with high-grade of metamorphism (see Fig. 1). Polishing was carefully done in order to avoid any possible fluctuation caused by surface roughness, since the methodology used in the assessment of concentrations is based on the approximation of flat samples with normal incidence for the correction of matrix effects [1,24]. Five monazite grains were characterized from this thin section.

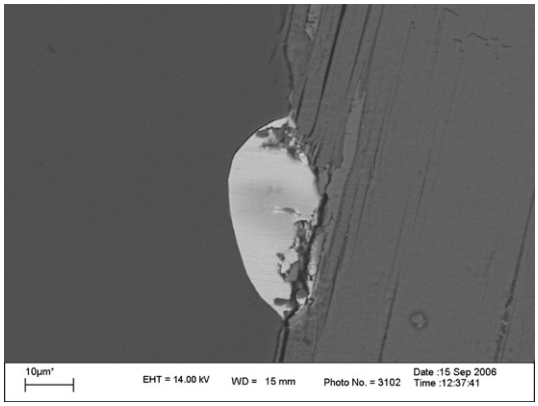


**Fig. 1.** Backscattered electron micrograph of a rock thin section with a monazite grain in the central region.

### 2.1. Data acquisition

The equipment used consists of a LEO 1450VP scanning electron microscope furnished with an INCA WAVE 700 wavelength dispersive spectrometer (WDS), from the Laboratorio de Microscopía Electrónica y Microanálisis (LABMEM) of the Universidad Nacional de San Luis, Argentina. The WDS detector has a Johansson geometry for the LiF, PET and TAP analyzer crystals, and a Johann geometry for the LSM60 and LSM200 ones, and two proportional counters configured in tandem in order to increase the efficiency at high energies: a P10 (90% Ar–10% $CH_4$) gas flow counter and a sealed one filled with Xe.

With the aim of performing a careful qualitative examination of possible overlappings, X-ray spectra were acquired from an unknown monazite grain, labeled here as grain #4, of the thin section studied. This grain was chosen for this study since it is quite large, and has an important number of trace elements (e.g. Pb and U), which usually constitute a difficulty for quantitative analysis [25]. Commercial SPI® mineral and pure metal standards were also measured, in order to cover all the elements detected in the monazite unknown sample: monazite standard for La, Ce, Pr, and Nd; apatite standard for P and Ca; quartz standard for Si and O; garnet standard for Y; pyrite standard for Fe and S; and Mg, Al, Mn, Zr, Pb, Th and U pure standards. Spectra were acquired in the most favorable angular range for each crystal (see Table 1), trying to attain the most adequate measuring conditions for achieving good statistics, appropriately exciting all elements with moderately high incident potential energy so that the interaction volume remains reduced, avoiding strong distortions in the assessment of matrix effects. For these reasons, electron incident energy was set to 15 keV, a collimator slit size of 2.5 mm and beam current around 100 nA being chosen in all cases.

Different scanning speeds were chosen so that acquisition times were not extremely long, and in the unknown samples a lower speed was used in order to achieve good statistics and thus clearly see all the elements present. Table 2 summarizes the measurement conditions for each sample.

When carrying out the measurement process, two important issues must be taken into account regarding image magnification. On the one hand, the magnification must be high enough in order to avoid

**Table 1**
Characteristics of the crystals used for spectrum acquisition, indicating the double interplanar distance ($2d$), and the ranges for angle $\theta$ and wavelength λ in each case.

| | $2d$ (nm) | $\theta$ range (°) | λ range (nm) |
|---|---|---|---|
| LiF | 0.40267 | 16.50–38.06 | 0.11436–0.24827 |
| PET | 0.8742 | 16.50–57.83 | 0.24828–0.74000 |
| TAP | 2.575 | 16.70–67.49 | 0.74001–2.37886 |
| LSM60 | 6 | 16.44–69.91 | 1.698–5.635 |

**Table 2**
Crystals and scan speeds used to acquire the WDS spectra for standards and unknown sample. Scan speeds are labeled according to the detector preset: 2 for 336 s/deg, 4 for 84 s/deg and 5 for 42 s/deg. Incident beam spot sizes chosen are also displayed.

| Sample | Scan speed | | | Spot size (nm) |
|---|---|---|---|---|
| | TAP | PET | LiF | |
| Unknown | 2 | 2 | 2 | 730 |
| Monazite | 5 | 5 | 4 | 700 |
| Apatite | – | 5 | – | 700 |
| Quartz | – | 5 | – | 700 |
| Pyrite | – | 5 | 4 | 700 |
| Garnet | 5 | 5 | – | 700 |
| Pb | – | 5 | – | 700 |
| Th | – | 5 | – | 700 |
| U | – | 5 | – | 700 |
| Al | 5 | – | – | 730 |
| Mg | 5 | – | – | 730 |
| Fe | – | – | 4 | 730 |
| Mn | – | – | 4 | 730 |
| Zr | – | 5 | – | 730 |

geometry effects: when using a low magnification value, a fraction of the scanned area is out of the Rowland circle, and therefore, the corresponding X-rays cannot reach the counters of the WDS; low magnifications may result in deformation of the peaks in a spectrum, expanding them and reducing their heights, measured intensities therefore resulting lower than in the appropriate geometry. On the other hand, the magnification must not be excessively high as to deliver an important radiative power in a very small region of the sample, in order to avoid electric charging and noticeable damage in the irradiated area [21]. A compromise must be sought for each case, and in the present work suitable magnifications were chosen in the range of 10,000× to 20,000×.

Since the continuum below peaks has different behaviours in the spectra acquired, background was subtracted from them using the program PeakFit®. Next, for each analyzer crystal, spectra were superimposed in different graphs in order to perform a careful qualitative analysis by observing all the possible peak interferences. From this careful examination, the most adequate experimental conditions for the quantifications were determined, i.e., decay lines to be measured, peak positions, wavelengths to be used for background subtraction, acquisition times, probe currents, etc.

Once the best experimental conditions for the measurements were established, characteristic and background intensities were registered at the selected angular positions, in order to carry out the quantification of the unknown monazite grains.

In order to account for matrix corrections and therefore to obtain sample compositions, the INCA Wave software which commands the WDS spectrometer was used. All cases were analyzed through two schemes: on the one hand, oxygen was quantified using its K$\alpha$ peak in both sample and standard; on the other hand, oxygen concentration was inferred by stoichiometry in the different oxides present in the mineral — in the case of Fe, the different oxidation states (FeO and $Fe_2O_3$) will not influence the global results, since Fe is present in very low concentrations.

## 3. Results and discussion

In the analysis of monazite samples, as in many other minerals, a significant number of elements is present, and care must be taken with the potential overlaps that may occur specifically in the main emission line used for the analysis of each element. Usually, the lines that interfere are weak or correspond to second or third diffraction orders in the analyzer crystal. The following is a detailed analysis for each of the elements present in the monazite sample which may exhibit interferences with other elements. This analysis is performed taking into account different WDS X-ray spectral regions, for which the background was first subtracted in order to perform a comparison by superposition of spectra. Peak identification has carefully been accomplished with the aid of values tabulated by Bearden [26]; in the case of satellite lines, different sources were used for wavelength identification [27,28].

Bearing in mind that most continuum spectra intervals surrounding a peak are approximately linear functions, the background is adequately evaluated by measuring two points, one on the left of a single peak or a group of peaks, and another one on the right, so that a straight line can be determined. The choice of where these points must be taken depends on the examination of all the peaks present in each region, and also on the background behaviour observed. This background point selection has to be decided in order to ensure that at these points no element peak is likely to appear, which would influence the background estimation, and correspondingly, the measured characteristic intensities. Since in most cases, the behaviour of the continuum spectrum is linear in intervals containing several peaks, the same background measurements have been used for different characteristic lines. In some cases, such as Al, Mg, Ce and La, the background may depart from a linear behaviour, so that the starting and ending background points were chosen as close to the peaks as possible. This nonlinear behaviour of the continuum spectrum cannot be observed in the graphs shown below since background has already been subtracted in them. However, the zero mean value of the background remainder guarantees the successful continuum subtraction. The points chosen with the purpose of estimating the background under all element peaks are displayed in Table 3.

For each element, a detailed analysis of possible overlaps was carried out in order to choose which peak should be used for quantification. In principle, the most intense line of the element is observed, and if it exhibits no significant overlapping effects, then it is chosen for quantification. Such are the cases for which the K$\alpha$ line is considered, since the K$\beta$ intensity is an order of magnitude lower and statistical fluctuations correspondingly become more remarkable. On the contrary, if overlapping effects for the most intense line are important, the following most intense peak is examined, and if this is free of noticeable neighbouring peaks, it is to be used for quantification despite its lower intensity. This situation was observed for some of the elements in which L or M emission lines were considered: in these cases, the decrease in the number of counts in second most intense peaks is not so drastic (see Table 4).

**Table 3**
Emission lines, analyzer crystals, wavelengths, beginning and ending background points for each continuum interval ($\lambda_{B-}$ and $\lambda_{B+}$, respectively), standards used and acquisition time for each peak and background measurement.

| Element | Line | Crystal | λ (nm) | $\lambda_{B-}$ (nm) | $\lambda_{B+}$ (nm) | Standard | Live time (s) |
|---|---|---|---|---|---|---|---|
| O | K$\alpha_{1,2}$ | LSM60 | 2.3790 | 2.2 | 2.6 | Quartz | 30 |
| Mg | K$\alpha_{1,2}$ | TAP | 0.9890 | 0.910 | 1.09 | Mg | 60 |
| Al | K$\alpha_{1,2}$ | TAP | 0.8340 | 0.775 | 0.866 | Al | 60 |
| Si | K$\alpha_{1,2}$ | PET | 0.7126 | 0.630 | 0.726 | Quartz | 60 |
| P | K$\alpha_{1,2}$ | PET | 0.6158 | 0.547 | 0.630 | Apatite | 30 |
| S | K$\alpha_{1,2}$ | PET | 0.5373 | 0.480 | 0.547 | Pyrite | 60 |
| Ca | K$\alpha_{1,2}$ | PET | 0.3360 | 0.322 | 0.360 | Apatite | 30 |
| Mn | K$\alpha_{1,2}$ | LiF | 0.2103 | 0.162 | 0.2237 | Mn | 60 |
| Fe | K$\alpha_{1,2}$ | LiF | 0.1937 | 0.162 | 0.2237 | Pyrite | 60 |
| Y | L$\alpha_{1,2}$ | PET | 0.6450 | 0.630 | 0.726 | Garnet | 60 |
| Zr | L$\alpha_{1,2}$ | PET | 0.6071 | 0.547 | 0.630 | Zr | 60 |
| La | L$\alpha_{1,2}$ | PET | 0.2666 | 0.25 | 0.272 | Monazite | 30 |
| Ce | L$\alpha_{1,2}$ | PET | 0.2564 | 0.25 | 0.272 | Monazite | 30 |
| Pr | L$\beta_1$ | LiF | 0.2258 | 0.2237 | 0.233 | Monazite | 40 |
| Nd | L$\beta_1$ | LiF | 0.2167 | 0.162 | 0.2237 | Monazite | 40 |
| Pb | M$\beta$ | PET | 0.5076 | 0.480 | 0.547 | Pb | 100 |
| Th | M$\alpha_{1,2}$ | PET | 0.4145 | 0.360 | 0.425 | Th | 30 |
| U | M$\beta$ | PET | 0.3716 | 0.360 | 0.425 | U | 100 |

**Table 4**
Line overlapping magnitudes found for the most intense lines of the elements present in the monazite (Mz.) samples analyzed. Line intensities are given in counts per second per nA (cps/nA) in order to illustrate the statistics governing each peak acquisition. Wavelengths λ for the main lines are given, as well as an idea of the overlapping occurring with other lines of wavelength $\lambda_I$. Relative interfering line intensities are taken from ref. [22].

| Element | Line | λ (nm) | Mz. grain (cps/nA) | Interfering line | $\lambda_I$ (nm) | Relative intensity | Interfering intensity (cps/nA) | Figure |
|---|---|---|---|---|---|---|---|---|
| S | K$\alpha_{1,2}$ | 0.53731 | 0.022 | Zr-L$\gamma_1$ | 0.53843 | 0.7% of Zr-L$\alpha_{1,2}$ | 0.0003 | 2 |
| | | | | Th-M$\zeta_2$ | 0.534 | 0.6% of Th-M$\alpha_{1,2}$ | 0.026 | |
| Ca | K$\alpha_{1,2}$ | 0.33595 | 6.497 | U-$M_2N_1$ | 0.3329 | 2% of U-M$\alpha_{1,2}$ | 0.012 | 5 |
| Mn | K$\alpha_{1,2}$ | 0.21031 | 0.086 | Nd-L$\beta_3$ | 0.21268 | – | 0.71 | – |
| | | | | Pr-L$\beta_{2,15}$ | 0.21194 | 18% of Pr-L$\alpha_{1,2}$ | – | |
| | | | | Ce-L$\gamma_5$ | 0.21103 | 0.8% of Ce-L$\beta_1$ | 0.06 | |
| Fe | K$\alpha_{1,2}$ | 0.1937 | 0.094 | Nd-L$\gamma_5$ | 0.19355 | 0.7% of Nd-L$\beta_1$ | 0.026 | 4 |
| | | | | Pr-L$\gamma_8$ | 0.19362 | 0.1% of Pr-L$\beta_1$ | 0.0009 | |
| | | | | Pr-L$\gamma_1$ | 0.19611 | 17% of Pr-L$\beta_1$ | 0.14 | |
| | | | | Ce-L$\gamma_2$ | 0.19602 | 15% of Ce-L$\beta_3$ | 0.337 | |
| Zr | L$\alpha_{1,2}$ | 0.60705 | 0.05 | Y-L$\beta_3$ | 0.59832 | 5% of Y-L$\alpha_{1,2}$ | 0.058 | 6 |
| | | | | Y-L$\beta_4$ | 0.60186 | 2.5% of Y-L$\alpha_{1,2}$ | 0.029 | |
| La | L$\alpha_{1,2}$ | 0.26657 | 26.023 | Nd-L↕ | 0.2676 | 8% of Nd-L$\alpha_{1,2}$ | 0.53 | – |
| | L$\beta_1$ | 0.245891 | ND | Pr-L$\alpha_{1,2}$ | 0.2463 | – | ND | – |
| | L$\beta_3$ | 0.24105 | 1.09 | Nd-L$\eta$ | 0.24094 | 0.7% of Nd-L$\beta_1$ | 0.026 | – |
| Pr | L$\alpha_{1,2}$ | 0.2463 | ND | La-L$\beta_1$ | 0.245891 | – | ND | – |
| Nd | L$\beta_1$ | 0.21668 | 3.59 | Ce-L$\beta_7$ | 0.21701 | 0.14% of Ce-L$\alpha_{1,2}$ | 0.042 | – |
| | L$\alpha_{1,2}$ | 0.23704 | 6.42 | La-L$\beta_6$ | 0.2379 | 0.9% of La-L$\alpha_{1,2}$ | 0.237 | – |
| | | | | Ce-L$\beta_1$ | 0.23561 | – | 7.98 | |
| Pb | M$\alpha_{1,2}$ | 0.5286 | 0.08 | Y-L$\gamma_{2,3}$ | 0.5283 | 2% of Y-L$\alpha_{1,2}$ | 0.023 | 2, 3 |
| | | | | Th-M$\zeta_1$ | 0.5245 | 1% of Th-M$\alpha_{1,2}$ | 0.043 | |
| | M$\beta$ | 0.5076 | 0.058 | U-M$\zeta_2$ | 0.505 | 0.5% of U-M$\alpha_{1,2}$ | 0.004 | 2 |
| | | | | S-K$\beta'$ | 0.5085 | 0.5% of S-K$\alpha_{1,2}$ | 0.0001 | |
| U | M$\beta$ | 0.3716 | 0.612 | Th-M$\gamma$ | 0.3679 | 5% of Th-M$\alpha_{1,2}$ | 0.217 | 5 |
| | M$\alpha_{1,2}$ | 0.391 | 0.765 | Th-M$\beta$ | 0.3941 | 75% of Th-M$\alpha_{1,2}$ | 3.275 | |

Special attention has been paid to the analysis of the peaks from Th, U and particularly Pb, as they occur in very low concentrations. The Pb-M$\beta$ line (0.5076 nm) has been chosen in this case, instead of Pb-M$\alpha_{1,2}$ (0.5286 nm), though this latter is more intense (approximately 1.4 times the intensity of the Pb-M$\beta$ line). This choice was made because the Pb-M$\alpha_{1,2}$ line coincides with the Y-L$\gamma_{2,3}$ line (0.5283 nm) (Figs. 2 and 3), and the Th-M$\zeta_1$ peak (0.5245 nm) appears quite close to the left, corresponding to around 1% of the Th-M$\alpha_{1,2}$ line. Yttrium is very likely to be found in most monazite grains, and its L$\gamma_{2,3}$ line can contribute to the intensity of the Pb-M$\alpha_{1,2}$; however, the Y-L$\gamma_{2,3}$ line is about 2% of the Y-L$\alpha_{1,2}$ line (0.6450 nm), which is the most intense emitted by this element. The Pb-M$\beta$ line is interfered by the U-M$\zeta_2$ line (0.5050 nm), whose intensity represents about 0.5% of the U-M$\alpha$ line (0.3910 nm), the most intense U characteristic line; however, this U-M$\zeta_2$ does not exactly coincide with the Pb-M$\beta$ line, and due to the U minor concentration, this interference does not represent a real problem. Sulphur contributes with its K$\beta'$ line at 0.5085 nm, quite close to the Pb-M$\beta$ line but with a very small intensity, representing 0.5% of S-K$\alpha_{1,2}$ (0.53731 nm), but sulphur concentration in monazite is very small — in Fig. 2, the line appears because the $FeS_2$ standard was used.

Also of interest is the case of Fe (Fig. 4), for which the K$\alpha_{1,2}$ line (0.1937 nm) exhibits overlapping with Nd-L$\gamma_5$ (0.19355 nm), approximately 0.7% of Nd-L$\beta_1$ (0.21668 nm), and with Pr-L$\gamma_8$ (0.19362 nm), which amounts to around 0.1% of Pr-L$\beta_1$ (0.22588 nm), as well as interferences with Pr-L$\gamma_1$ (0.19611 nm), approximately 17% of Pr-L$\beta_1$ (0.22588 nm), and Ce-L$\gamma_2$ (0.19602 nm), around 15% the intensity of Ce-L$\beta_3$ (0.23109 nm). Despite these potential interferences, the Fe-K$\alpha_{1,2}$ line has to be chosen, since the Fe-K$\beta_{1,3}$ line (0.17566 nm) only amounts 17% of the K$\alpha_{1,2}$, and only traces of Fe are present in the samples analyzed.

Figs. 2 to 7 show the spectral regions surrounding those peaks selected for performing the analysis which exhibit overlappings that may distort the measurements. Fig. 7 displays second and third order diffraction peaks from the analyzer crystal, which can always be avoided by means of an energy discriminator window in the proportional

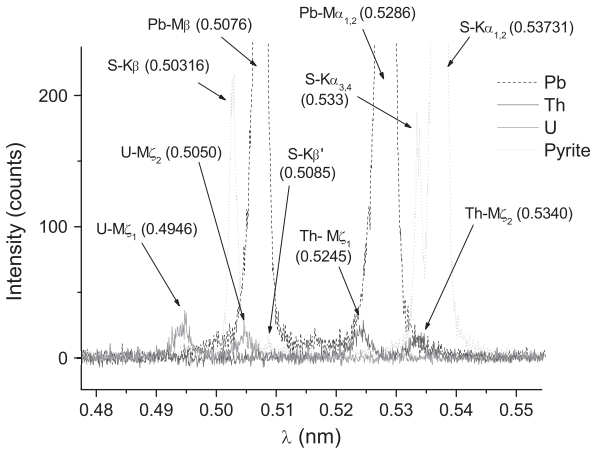


**Fig. 2.** Spectra obtained from Pb, Th, U and pyrite standards, in the range 0.475 nm to 0.555 nm of the PET crystal. Quantifications were carried out considering Pb-M$\beta$ (0.5076 nm) and Si-K$\alpha_{1,2}$ (0.53731 nm) peaks.

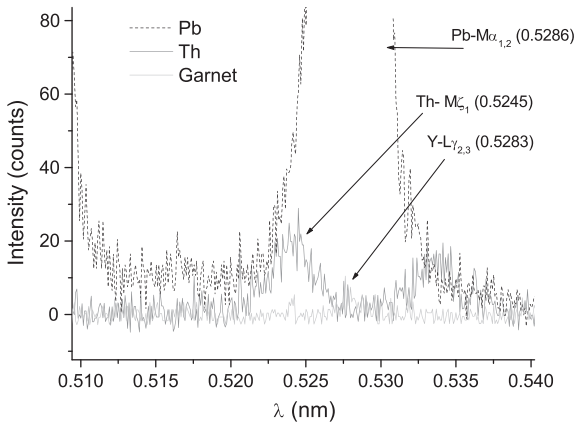


**Fig. 3.** Spectra obtained from Pb, Th and garnet standards, in the range 0.510 nm to 0.540 nm of the PET crystal. Main overlaps in this region are pointed.

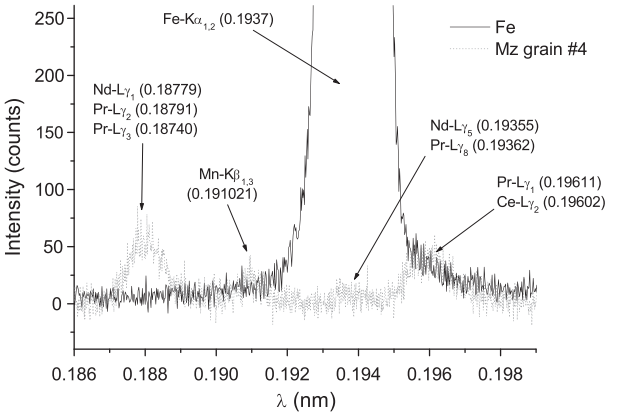


**Fig. 4.** Spectra obtained from monazite grain #4 and Fe standard, in the range 0.186 to 0.199 nm of the LiF crystal. Quantifications were carried out considering Fe-K$\alpha$ (0.1937 nm).

counter of the WDS. All the overlappings for each element are summarized in Table 4; the interfering line intensities relative to the most intense line of the corresponding interfering group are also shown, according to the radiative transition rates provided by Perkins et al. [22].

It is worth noticing that although some interferences may at first sight appear as important, they will imply no relevancy in the quantification procedure, due to the concentration relationships for the elements involved.

After this careful qualitative analysis of all spectra involved, the elements present in the monazite grain are brought to evidence, and are measurable with this spectrometer for concentrations greater than around 100 ppm. Experimental conditions were then defined for all elements: emission lines chosen, analyzing crystal, wavelengths for background acquisition, etc., which are summarized in Table 3. As detailed before, the acquisition live times displayed in this table were established according to each peak intensity so that statistical fluctuations do not influence the measurements, and standards with appropriate stoichiometric stability were selected when possible.

Once the most adequate experimental conditions have clearly been defined for each element, the monazite grains and monazite standard were analyzed. To this purpose, the beam current chosen, up to around 100 nA, is a reasonable value in order not to produce sample overheating, which may result in measurement distortions and specimen damage.

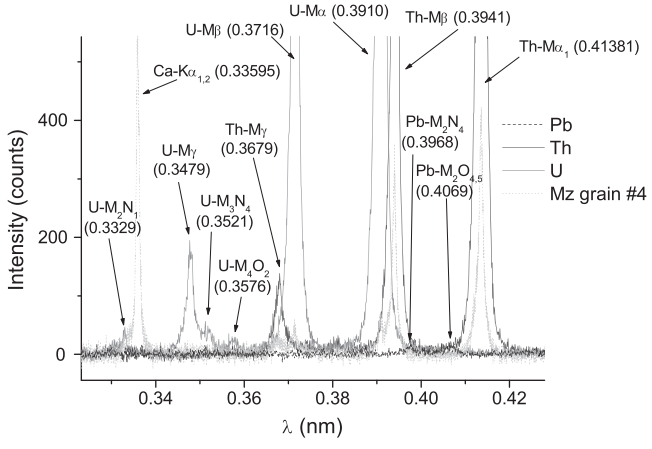


**Fig. 5.** Spectra obtained from monazite grain #4 and Th, U and Pb standards, in the range 0.325 nm to 0.425 nm of the PET crystal. Quantifications were carried out considering U-M$\beta$ (0.3716 nm), Th-M$\alpha_1$ (0.41381 nm) and Ca-$K_{1,2}$ (0.33595 nm) peaks.

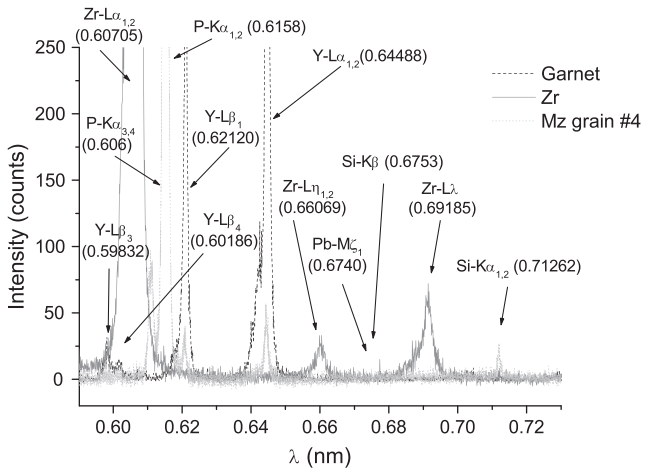


**Fig. 6.** Spectra obtained from monazite grain #4 and garnet and Zr standards, in the range 0.590 nm to 0.730 nm of the PET crystal. Quantifications were carried out considering Zr-L$\alpha_{1,2}$ (0.6070 nm), P-K$\alpha_{1,2}$ (0.6158 nm) and Y-L$\alpha_{1,2}$ (0.64488 nm) peaks.

As mentioned above, all cases were analyzed through two schemes: quantifying oxygen through its K$\alpha$ peak, or inferring oxygen concentration by stoichiometry in the different oxides present. This second strategy would allow to overcome the problem of performing compositional analysis using the O-K$\alpha$ line, whose intensity is determined with serious complications [29–31]. The corresponding results are displayed in Table 5. It can be seen that, despite the inconveniences pointed, the results obtained for the quantification of the grains studied are apparently more reliable when selecting isolated elements instead of oxides.

It is worth mentioning that the elemental concentrations of the unknown grains must not be similar to those corresponding to the monazite standard. Regarding the characterization of Fe, it is important to remark that in grain no. 3 this element was not detected. Bearing in mind that the Nd content in this grain is important as compared to the other grains, a noticeable distortion in the Fe-K$\alpha_{1,2}$ intensity measured might be expected, if the Nd-L$\gamma_5$ line (and also Pr-L$\gamma_8$) would seriously interfere this line, which is used for Fe quantification. However, evidently no distortion occurs, since in that case some spurious Fe-K$\alpha_{1,2}$ intensity would be measured, providing an erroneous Fe content in this grain, which actually does not occur. This fact supports the choice of the Fe-K$\alpha_{1,2}$ line for achieving an appropriate determination of this element.

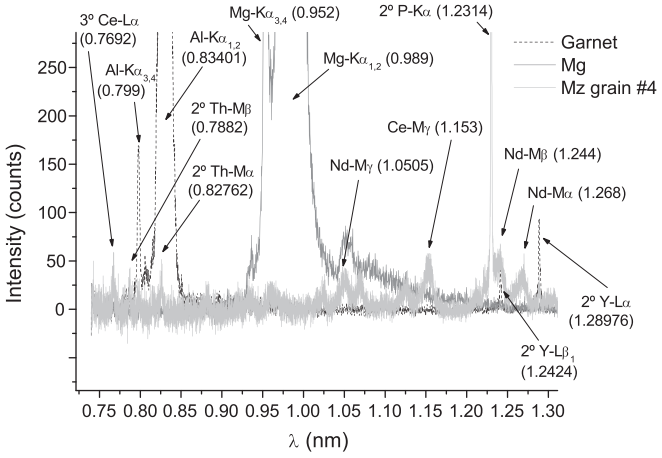


**Fig. 7.** Spectra obtained from monazite grain #4, garnet and Mg standards, in the range 0.721 nm to 1.311 of the TAP crystal. Quantifications were carried out considering Al-K$\alpha_{1,2}$ (0.8340 nm) and Mg-K$\alpha_{1,2}$ (0.9890 nm) peaks.

**Table 5**
Weight percent concentrations obtained for the monazite (Mz.) standard and five unknown monazite grains. Each first line shows the results obtained by using the O-K$\alpha$ peak, whereas second lines correspond to the oxygen concentrations obtained by stoichiometry. Numbers in parentheses represent the estimated uncertainties in the last digit.

| Element | Mz. standard nominal | Mz. standard measured | Grain #1 | Grain #2 | Grain #3 | Grain #4 | Grain #5 |
|---|---|---|---|---|---|---|---|
| Mg | – | – | 0.003(1) | 0.017(1) | – | – | – |
| | | | 0.003(1) | 0.017(1) | – | – | – |
| Al | – | – | 0.003(1) | 0.036(1) | 0.026(1) | 0.032(1) | 0.001(1) |
| | | | 0.003(1) | 0.036(1) | 0.025(1) | 0.032(1) | 0.001(1) |
| Si | – | – | 0.132(3) | 0.175(3) | 0.133(3) | 0.161(3) | 0.354(5) |
| | | | 0.132(3) | 0.174(3) | 0.132(3) | 0.160(3) | 0.353(5) |
| P | 12.1 | 12.24(5) | 13.56(5) | 13.49(5) | 12.73(5) | 12.44(5) | 12.69(6) |
| | | 12.75(5) | 13.51(5) | 13.45(5) | 12.69(5) | 12.40(5) | 12.66(6) |
| S | – | – | 0.005(2) | 0.008(2) | 0.002(2) | 0.001(2) | 0.216(3) |
| | | | 0.005(2) | 0.008(2) | 0.002(2) | 0.001(2) | 0.215(3) |
| Ca | 0.40 | 0.391(5) | 0.694(5) | 0.665(5) | 0.603(4) | 0.660(4) | 0.388(5) |
| | | 0.393(5) | 0.765(5) | 0.730(6) | 0.603(4) | 0.726(4) | 0.427(5) |
| Mn | – | – | 0.058(7) | 0.048(7) | 0.055(6) | 0.056(6) | 0.016(7) |
| | | | 0.058(7) | 0.048(7) | 0.055(6) | 0.057(6) | 0.016(7) |
| Fe | – | – | 0.062(7) | 0.251(8) | – | 0.008(6) | 0.069(7) |
| | | – | 0.063(7) | 0.252(8) | – | 0.008(6) | 0.069(7) |
| Y | – | – | 1.68(2) | 0.74(1) | 1.62(2) | 1.82(2) | 0.41(1) |
| | | | 1.67(2) | 0.74(1) | 1.62(2) | 1.82(2) | 0.41(1) |
| Zr | – | – | 0.077(7) | 0.064(7) | 0.065(7) | 0.067(7) | 0.071(8) |
| | | | 0.077(7) | 0.064(7) | 0.064(7) | 0.067(7) | 0.071(8) |
| La | 12.90 | 13.05(5) | 10.27(4) | 11.15(5) | 11.67(5) | 11.44(5) | 14.71(6) |
| | | 11.38(5) | 10.38(4) | 11.19(5) | 11.75(5) | 11.54(5) | 14.78(6) |
| Ce | 30.80 | 30.76(7) | 24.55(6) | 26.22(6) | 25.55(6) | 25.64(6) | 30.32(8) |
| | | 31.13(7) | 25.19(6) | 26.70(6) | 26.10(6) | 26.24(6) | 30.92(8) |
| Pr | 4.20 | 4.2(1) | 3.9(1) | 4.1(1) | 4.1(1) | 3.9(1) | 4.1(1) |
| | | 4.3(1) | 4.0(1) | 4.2(1) | 4.2(1) | 4.0(1) | 4.0(1) |
| Nd | 8.70 | 8.9(1) | 9.8(1) | 9.9(1) | 9.9(1) | 9.8(1) | 8.5(1) |
| | | 9.1(1) | 9.8(1) | 9.8(1) | 9.9(1) | 9.8(1) | 8.4(1) |
| Pb | – | – | 0.14(1) | 0.13(1) | 0.15(1) | 0.15(1) | 0.27(1) |
| | | | 0.14(1) | 0.13(1) | 0.15(1) | 0.15(1) | 0.27(1) |
| Th | 3.80 | 3.86(5) | 3.53(3) | 3.97(3) | 3.49(3) | 4.01(3) | 2.90(3) |
| | | 3.92(5) | 4.46(4) | 5.01(4) | 4.41(3) | 5.07(4) | 3.66(4) |
| U | – | – | 0.57(1) | 0.435(9) | 0.72(1) | 0.58(1) | 0.038(8) |
| | | | 0.57(1) | 0.436(9) | 0.72(1) | 0.58(1) | 0.038(8) |
| O | 25.9 | 26.4(2) | 22.5(2) | 26.0(2) | 23.9(2) | 22.8(2) | 25.4(2) |
| | | 26.70(9) | 27.6(1) | 27.9(1) | 26.9(1) | 26.68(9) | 27.9(1) |
| Total | 98.8 | 99.8(3) | 91.5 | 97.3 | 94.7 | 93.6 | 100.4 |
| | | 99.6(2) | 98.4 | 100.9 | 99.4 | 99.3 | 104.3 |

In Table 5 important differences can be observed for Th contents when quantifying it as a single element or as oxide. However it must be borne in mind that phosphorus is an efficient absorber for Th M-lines, which may introduce considerable systematic errors in the quantification routine used.

## 4. Conclusions

EPMA X-ray emission from monazite samples was studied in a scanning electron microscope, with a wavelength dispersive spectrometer attached. A careful spectral inspection has given place to the identification of angular positions of the most adequate peaks for performing quantitative analysis, allowing to avoid important overlappings which may hinder the quantification procedures. The good WDS energy resolution is indispensable for this kind of analysis, which implies good peak-to-background ratios and therefore better detection limits. It has been shown that the choice of the Pb-M$\beta$ line renders a reliable quantification, despite the fact that it is less intense than the Pb-M$\alpha_{1,2}$ line, usually used in the characterization of monazites.

In the analysis of monazite samples, the incident beam energy should not exceed 15 keV, since an efficient excitation of all lines of interest is achieved without strongly enlarging the size of the interaction volume. This allows a good spatial resolution, which is a very important issue when zonations and grain analysis are to be faced, as usually occurs in geochronological studies.

## Acknowledgements

This work was financially supported by the Secretaría de Ciencia y Técnica of the Universidad Nacional de San Luis, to whom the authors gratefully acknowledge. They are also thankful for the financial support from CONICET, in the frame of PIP 6310.

## References

[1] S. Reed, Electron Probe Microanalysis, 2nd ed. Cambridge University Press, Cambridge, 1993.
[2] V. Scott, G. Love, S. Reed, Quantitative Electron-Probe Microanalysis, 2a. ed. Ellis Horwood Ltd., Nueva York, 1995.
[3] J. Goldstein, D. Newbury, P. Echlin, D. Joy, A. Romig, C. Lyman, C. Fiori, E. Lifshin, Scanning Electron Microscopy and X-ray Microanalysis: A Text for Biologists, Materials Scientists, and Geologists, Plenum Press, New York, 1992.
[4] L. Reimer, Scanning electron microscopy: physics of image formation and microanalysis, in: P. Hawkes (Ed.), Springer Series in Optical Sciences. 2nd ed., 1998.
[5] E. Krefting, M. Felsmann, A. Recker, B. Feja, H. Hohling, R. Reichelt, L. Reimer, Spatial resolution of electron probe X-ray microanalysis on sections of organic (biological) material, Ultramicroscopy 77 (1999) 13–21.
[6] S. Brémier, D. Haas, J. Somers, C. Walker, Large area quantitative X-ray mapping of (U, Pu)$O_2$ nuclear fuel pellets using wavelength dispersive electron probe microanalysis, Spectrochim. Acta Part B 58 (2003) 651–658.
[7] Y. Lin, J. Duh, Phase transformation of the phosphorus-rich layer in SnAgCu/Ni–P solder joints, Scr. Mater. 54 (2006) 1661–1665.
[8] Z. Samardžija, J. Jeon, M. Čeh, Microstructural and compositional study of a bulk Pb($Mg_{1/3}Nb_{2/3}$) $O_3$–$PbTiO_3$ single crystal grown from a $BaTiO_3$ seed, Mater. Charact. 58 (2007) 534–543.
[9] A. Cocherie, O. Legendre, J.J. Peucat, A.N. Kouamelan, Geochronology of polygenetic monazites constrained by in situ electron microprobe Th–U-total

lead determination: implications for lead behaviour in monazite, Geochim. Cosmochim. Acta 62 (1998) 2475–2497.
[10] J. Pyle, F. Spear, D. Wark, C. Daniel, L. Storm, Contributions to precision and accuracy of monazite microprobe ages, Am. Mineralog. 90 (2005) 547–577.
[11] R. Parrish, U–Pb dating of monazite and its application to geological problems, Can. J. Earth Sci. 27 (1990) 1431–1450.
[12] M.L. Williams, M.J. Jercinovic, Microprobe monazite geochronology: putting absolute time into microstructural analysis, J. Struct. Geol. 24 (2002) 1013–1028.
[13] A. Cocherie, F. Albarede, An improved U–Th–Pb age calculation for electron microprobe dating of monazite, Geochim. Cosmochim. Acta 65 (2001) 4509–4522.
[14] J.F. Silvain, M.R. Turner, M. Lahaye, Comparative AES and EPMA studies of diffusion profiles of Al–Au–C and AS7GO.6–Au–C interfaces, Compos. A 27A (1996) 793–798.
[15] J.L. Crowley, E.D. Ghent, An electron microprobe study of the U–Th–Pb systematics of metamorphosed monazite: the role of Pb diffusion versus overgrowth and recrystallization, Chem. Geol. 157 (1999) 285–302.
[16] D. Newbury, Microanalysis to nanoanalysis: measuring composition at high spatial resolution, Nanotechnology 1 (1990) 103–130.
[17] G. Love, V.D. Scott, Phase identification of microfeatures using EPMA methods, especially high-resolution X-ray spectroscopy, Micron 32 (2001) 115–128.
[18] D. Newbury, Barriers to quantitative electron probe X-ray microanalysis for low voltage scanning electron microscopy, J. Res. Nat. Inst. Stand. Technol. 107 (2002) 605–619.
[19] M. Tanaka, M. Takeguchi, K. Furuya, X-ray analysis and mapping by wavelength dispersive X-ray spectroscopy in an electron microscope, Ultramicroscopy 108 (2008) 1427–1431.
[20] I. Braun, J.M. Montel, C. Nicollet, Electron microprobe dating of monazites from high-grade gneisses and pegmatites from the Kerala Kondalite Belt, southern India, Chem. Geol. 146 (1998) 65–85.
[21] M. Jercinovic, M. Williams, Analytical perils (and progress) in electron microprobe trace element analysis applied to geochronology: background acquisition, interferences, and beam irradiation effects, Am. Mineralog. 90 (2005) 526–546.
[22] S.T. Perkins, D.E. Cullen, M.H. Chen, J.H. Hubbell, J. Rathkopf, J. Scofield, Tables and graphs of atomic subshells and relaxation data derived from LLNL evaluated atomic data library (EADL), Z = 1–100, Lawrence Livermore National Laboratory, Report UCRL-50400, vol. 30, 1991.
[23] A.B. Guereschi, R.D. Martino, Geotermobarometría de la paragénesis Qtz + Pl + Bt + Grt + Sil en gneises de alto grado del sector centro-oriental de la Sierra de Comechingones, Córdoba Rev. Asoc. Geológica Argent. 57 (2002) 365–375.
[24] P. Duncumb, Quantitative analysis with the electron microprobe. The first 50 years and beyond, J. Anal. At. Spectrom. 14 (1999) 357–366.
[25] N. Scherrer, M. Engi, E. Gnos, V. Jakob, A. Liechti, Monazite analysis; from sample preparation to microprobe age dating and REE quantification, Schweiz. Mineral. Petrogr. Mitt. 80 (2000) 93–105.
[26] J. Bearden, X-ray wavelengths, Rev. Mod. Phys. 39 (1967) 78–124.
[27] J. Kawai, Chemical effects in the satellites of X-ray emission spectra, Nucl. Instr. Meth. Phys. Res. B 75 (1993) 3–8.
[28] V. Horvat, R.L. Watson, Y. Peng, Systematics of Kα X-ray satellite structure, Phys. Rev. A At. Mol. Opt. Phys. 74 (2006) 022718.
[29] G. Bastin, H. Heijligers, Present and future of light element analysis with electron beam instruments, Microbeam Anal. 1 (1992) 61–73.
[30] J. Goldstein, S. Choi, F. Van Loo, H. Heijligers, G. Bastin, W. Sloof, The influence of oxide surface layers on bulk electron probe microanalysis of oxygen—application to Ti–Si–O compounds, Scanning 15 (1993) 165–170.
[31] S. Dreer, P. Wilhartitz, Critical evaluation of the state of the art of the analysis of light elements in thin films demonstrated using the examples of $SiO_xN_y$ and $AlO_xN_y$ films, Pure Appl. Chem. 76 (2004) 1161–1213.